IEEE Open Journal of
Power Electronics

Received 30 October 2022; revised 10 December 2022; accepted 18 December 2022. Date of publication 21 December 2022; date of current version 30 December 2022. The review of this article was arranged by Associate Editor Zhixiang Zou.

Digital Object Identifier 10.1109/OJPEL.2022.3230956

Online-Harmonic-Detection-Based System Stabilization Function for Grid-Forming Inverters Under Various Grid Conditions

LE KONG [1] (Member, IEEE), YAOSUO XUE [2] (Senior Member, IEEE), LIANG QIAO [1] (Student Member, IEEE), AND FEI GAE WANG [1,2] (Fellow, IEEE)

[1]EECS, University of Tennessee, Knoxville, TN 37996-2250 USA
[2]Oak Ridge National Laboratory, Oak Ridge, TN 37831 USA

CORRESPONDING AUTHOR: LE KONG (e-mail: lkong92@ieee.org)

This work was supported in part by the US Department of Energy, Office of Electricity, in part by Advanced Grid Modeling Program under Contract DE-AC05-00OR22725, in part by Engineering Research Center Shared Facilities through the Engineering Research Center Program of the National Science Foundation and the Department of Energy under NSF Award EEC1041877, and in part by the CURENT Industry Partnership Program.

ABSTRACT In power systems with grid-forming inverters (GFMs), small-signal instability issues could occur due to harmonic excitation, impedance interactions, and poor inverter control design. There mainly exist two types of stability issues based on the frequency range. One is the low-frequency resonance (0 – $2f_0$ Hz) and the other is the high-frequency harmonics (above $2f_0$ Hz), where f_0 is the system fundamental frequency. By assuming that the low-frequency related controls are well designed, this paper addresses the high-frequency harmonic issues. The goal is to develop a system stabilization function (SSF) to eliminate any high-frequency stability issues under various grid conditions without affecting predefined low-frequency behaviors. The idea is to conduct the inverter passivation test at the system harmonic resonant frequency so that the corresponding harmonic instability can be removed. To achieve this, the resonant frequency of the harmonic instability is detected first, and then if the magnitude of the resonant component exceeds the threshold value, the proposed SSF will be enabled, thus the system would be stabilized. Both simulation and experimental tests are conducted to validate the effectiveness of the proposed approach.

INDEX TERMS Grid-forming inverters, harmonic instability, online harmonic detection, passivity-based design.

I. INTRODUCTION

Grid-forming inverters (GFMs) can enable the stable operation of up to 100 % penetration of renewable resources for future power-electronics-based grids [1], [2]. A GFM normally has an inner ac voltage regulation loop and an outer power loop. The inner ac voltage loop can make the inverter act like a voltage source and thus can stably operate in weak systems. The outer power loop enables the inverter to synchronize with the rest of the grid. Typical outer power loop control methods of GFMs include the frequency droop control [3], [4], the virtual synchronous machine control (VSM) [5], and the dispatchable virtual oscillator control (dVOC) [6], [7], etc. These control loops in GFMs may interact with different impedances of the rest of the system and introduce small-signal stability issues into the grids [8], [9], [10]. The small-signal stability issues could be further categorized into two types according to the frequency range. One is the low-frequency resonance (0 – $2f_0$ Hz) which is mainly caused by the interactions between the grid and the outer power control of inverters; and the other is the high-frequency harmonic (above $2f_0$ Hz where f_0 is the system fundamental frequency) which is mainly introduced by the interactions between the grid and the voltage/current control, high-frequency filters, or control delays of the inverters. In this paper, it is assumed that

the outer power loops are well designed according to the grid conditions so that there are no low-frequency stability issues. Therefore, the focus of this paper will be on designing a smart inverter control [11] so that the high-frequency instability issues under different grid conditions can be eliminated.

The design of inverter control to enhance system harmonic stability under various grid conditions usually can be achieved by three types of approaches, including offline impedance reshaping or impedance passivation, online grid impedance measurement-based approach, and online harmonic detection-based approach [12]. The offline impedance reshaping is to add some passive or active damping into the GFMs to damp the possible oscillations in the system, and the offline impedance passivation is to design the inverter impedance to be passive so that it can be stably connected to any passive grid. So far, many stabilization approaches for high-frequency harmonic stability issues have been developed for grid-following inverters, such as control time delay compensation or phase compensation [13], [14], but few system stabilization methods have been developed for GFMs. In [15], a passivity-based design was proposed for GFMs by adding both virtual impedance control and capacitor voltage feedback decoupling control into the inner control loops for system stability enhancement. A similar discrete passivity-based approach has also been developed in [16]. However, it will be shown in detail later in Section III that with the virtual impedance control Z_v, although the high-frequency harmonics can be eliminated, the predefined low-frequency behaviors of GFMs might be affected and small-signal synchronization stability issues might occur. The online grid impedance measurement approach is to estimate the grid side impedance and then adjust the control parameters accordingly [17]. However, the grid impedance could be rather complicated which might be difficult to estimate accurately by simply assuming that the grid is a series connection of an inductor and a resistor. Since it is difficult to find a control approach to directly render the inverter impedance passive at high-frequency regions without affecting the predefined low-frequency dynamics, and the grid impedance measurement-based approach is not always feasible, the online resonance detection-based approach can be adopted. An online harmonic stability enhancement approach was proposed in [12] for GFMs by adding a phase compensation circuit with a notch filter on the current feedforward loop. However, the controller in [12] was only designed for a single-voltage-loop converter with a current feedforward loop, not a generalized inner double-loop control scheme with both voltage and current feedback control loops.

Therefore, this paper proposes an online harmonic detection-based system stabilization function for GFMs with inner double-loop control (i.e., voltage loop and current loop) scheme, which aims at improving the high-frequency stability of the system without affecting the predefined low-frequency dynamics. The rest of the paper is organized as follows. In Section II, the passivity analysis and system stability analysis under different grid conditions are conducted for the basic GFM control approach [4] based on the impedance models. Section III analyzes the potential issues of the existing passivity-based control approaches [15] for GFMs and proposes the online harmonic detection-based SSF. Section IV uses both simulations and experimental tests to validate the effectiveness of the proposed approach. Section V concludes the paper.

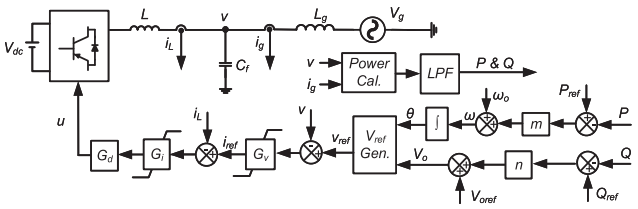

FIGURE 1. Circuit and control diagram of the basic GFM.

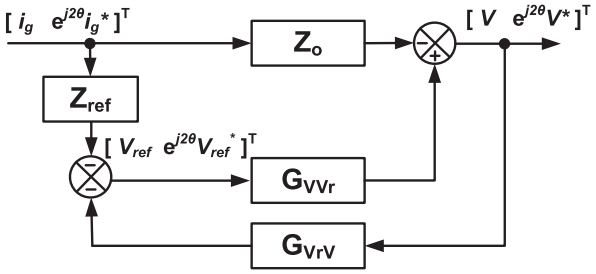

FIGURE 2. Full-order model of GFMs with control in Fig. 1 [18].

II. STABILITY ANALYSIS OF GFMS UNDER VARIOUS GRID CONDITIONS

The main circuit and control blocks of a widely used multi-loop GFM are shown in Fig. 1 [4]. In this circuit diagram, an *LC* filter is used to mitigate the switching ripples. The power control block is to generate the magnitude and phase angle of the voltage reference through the widely used droop control strategy, including an active power-frequency (*P-f*) droop control with frequency droop gain m and a reactive power-voltage (*Q-v*) droop control with voltage droop gain n. The voltage controller G_v is to regulate the output voltage, and the inner current controller G_i is to provide damping for the *LC* resonance and to limit the overcurrent. Control delay in the system (e.g., sampling delay, PWM delay, etc.) is integrated as the block G_d in the diagram. In addition, the voltage and current control loops can be implemented either in the *dq0* axis or $\alpha\beta 0$ axis. In this paper, the controller is implemented with voltage and current limiters in $\alpha\beta$ coordinates

A. IMPEDANCE MODEL OF GFMS

To analyze system stability, the impedance model of GFM can be used, such as the complex-value-based impedance model that is developed in [18]. The closed-loop model of the GFM considering the impacts of both the outer power control loop and the inner voltage and current loops can be obtained as in Fig. 2, which depicts the relationships among the grid side current i_g, output voltage v, reference voltage V_{ref}, and their

corresponding complex conjugate with a 2θ angle rotation ($e^{j2\theta}i_g^*$, $e^{j2\theta}v^*$, and $e^{j2\theta}v_{ref}^*$), where θ is the angle of steady-state voltage V_{dq} and current I_{dq} in the synchronous reference frame.

As seen in Fig. 2, the impacts of the outer power loop on voltage reference can be represented by two transfer function matrices: $\boldsymbol{G_{VrV}}$ which is from the output voltage to the reference voltage as shown in (1), and $\boldsymbol{Z_{ref}}$ which is from the output current to the reference voltage as shown in (2), with ω_0 being the system fundamental frequency and ω_c being the cut-off frequency of the low-pass filter for the measured power.

$$\boldsymbol{G_{VrV}} = \frac{j}{2}\begin{bmatrix} -H_1 I_{dq}^* & -H_2 I_{dq} \\ H_2 I_{dq}^* & H_1 I_{dq} \end{bmatrix} \tag{1}$$

$$\boldsymbol{Z_{ref}} = \frac{j}{2}\begin{bmatrix} -H_2 V_{dq}^* & -H_1 V_{dq} \\ H_1 V_{dq}^* & H_2 V_{dq} \end{bmatrix} \tag{2}$$

where,

$$H_1 = V_0 G_P(s - j\omega_0) - G_Q(s - j\omega_0) \tag{3}$$

$$H_2 = V_0 G_P(s - j\omega_0) + G_Q(s - j\omega_0) \tag{4}$$

$$G_P(s) = -\frac{\omega_c}{s+\omega_c}\frac{m}{s} \tag{5}$$

$$G_Q(s) = -\frac{\omega_c}{s+\omega_c}n \tag{6}$$

$$I_{dq}^* = I_d - jI_q,\ I_{dq} = I_d + jI_q \tag{7}$$

$$V_{dq}^* = V_d - jV_q,\ V_{dq} = V_d + jV_q \tag{8}$$

Additionally, $\boldsymbol{Z_o}$ is the full-order transfer function matrix considering the inner voltage and current loops as shown in (9), and $\boldsymbol{G_{VVr}}$ is the transfer function matrix from the reference voltage to the output voltage as given in (10).

$$\boldsymbol{Z_o}(s) = \begin{bmatrix} Z_{ov}(s) & 0 \\ 0 & Z_{ov}(s - 2j\omega_0) \end{bmatrix} \tag{9}$$

$$\boldsymbol{G_{VVr}}(s) = \begin{bmatrix} G_{vvr}(s) & 0 \\ 0 & G_{vvr}(s - 2j\omega_0) \end{bmatrix} \tag{10}$$

where,

$$Z_{ov}(s) = \frac{sL + G_i G_d}{LC_f s^2 + G_i G_d C_f s + G_v G_i G_d + 1} \tag{11}$$

$$G_{vvr}(s) = \frac{G_v G_i G_d}{LC_f s^2 + G_i G_d C_f s + G_v G_i G_d + 1} \tag{12}$$

With the four transfer function matrices in (1), (2), (9), and (10), the full impedance model of GFM ($\boldsymbol{Z_{o\_GFM\_1}}$) can be derived as a 2×2 multi-input-multi-output transfer function as shown in (13).

$$\boldsymbol{Z_{o\_GFM\_1}}(s) = (\boldsymbol{I} + \boldsymbol{G_{VVr}}\boldsymbol{G_{VrV}})^{-1}\left(\boldsymbol{Z_o} + \boldsymbol{G_{VVr}}\boldsymbol{Z_{ref}}\right) \tag{13}$$

Note that this model can be extended to other outer power control methods, such as dVOC or VSM, by replacing the P-θ relationship in (5) and the Q-V relationship in (6).

TABLE 1. Circuit and Control Parameters of GFMs and Grid Conditions

Variables	Value	Variables	Value
GFM voltage RMS value V_{oref}	130 V	Fundamental frequency f_0	60 Hz
Dc voltage V_{dc}	500 V	Switching frequency f_{sw}	10 kHz
LC filter capacitance L, C	2 mH, 10 μF	Power references P_{ref}, Q_{ref}	1 kW, 0 Var
Control delay T_d	$1.5/f_{sw}$	Current P control K_{pi}	8
Voltage PR control proportional gain K_{pv}	0.01	Voltage PR control resonance gain K_{rv}	50

Variables	Value				
Grid impedances L_g (mH)	8	6	4	3	2
Grid strength SCR	5.6	7.5	11	15	22
Frequency droop gain m (ω_0/P_0)	2%	2%	0.5%	0.3%	0.2%
Angle droop gain n (V_0/P_0)	10%	10%	2.5%	2%	1%

B. STABILITY ANALYSIS OF GFMS UNDER VARIOUS GRID CONDITIONS

For the grid-side model, the complex-value-based grid admittance can be modeled as (14). Then, the stability of the interconnected GFM and grid can be determined by checking the encirclement of (-1, $j0$) of the eigenvalues of the return ratio matrix $\boldsymbol{L}_1(s)$ and the number of right-half plane poles (RHP) of $\boldsymbol{L}_1(s)$, where $\boldsymbol{L}_1(s)$ is shown in (15).

$$\boldsymbol{Y_g}(s) = \begin{bmatrix} \frac{1}{sL_g} & 0 \\ 0 & \frac{1}{(s-2j\omega_0)L_g} \end{bmatrix} \tag{14}$$

$$\boldsymbol{L}_1(s) = \boldsymbol{Z_{o\_GFM\_1}}(s)\ \boldsymbol{Y_g}(s) \tag{15}$$

A case study is then conducted below to show the stability of GFMs under various grid conditions. The circuit and control parameters of GFMs and the grid conditions from the weak grid to the strong grid are shown in Table 1. A simple metric, short circuit ratio (SCR), is used here to briefly describe the grid strength. The larger SCR is, the stronger the grid will be. Note that the droop gains m and n are adjusted according to the grid strength to maintain system small-signal synchronization stability in the low-frequency region (i.e., near the system fundamental frequency).

Fig. 3 shows the impedance-based analysis results and the simulation results under SCR = 5.6. It can be seen that the system is stable and there are no harmonic instability issues. But when the grid impedance decreases, i.e., SCR increases,

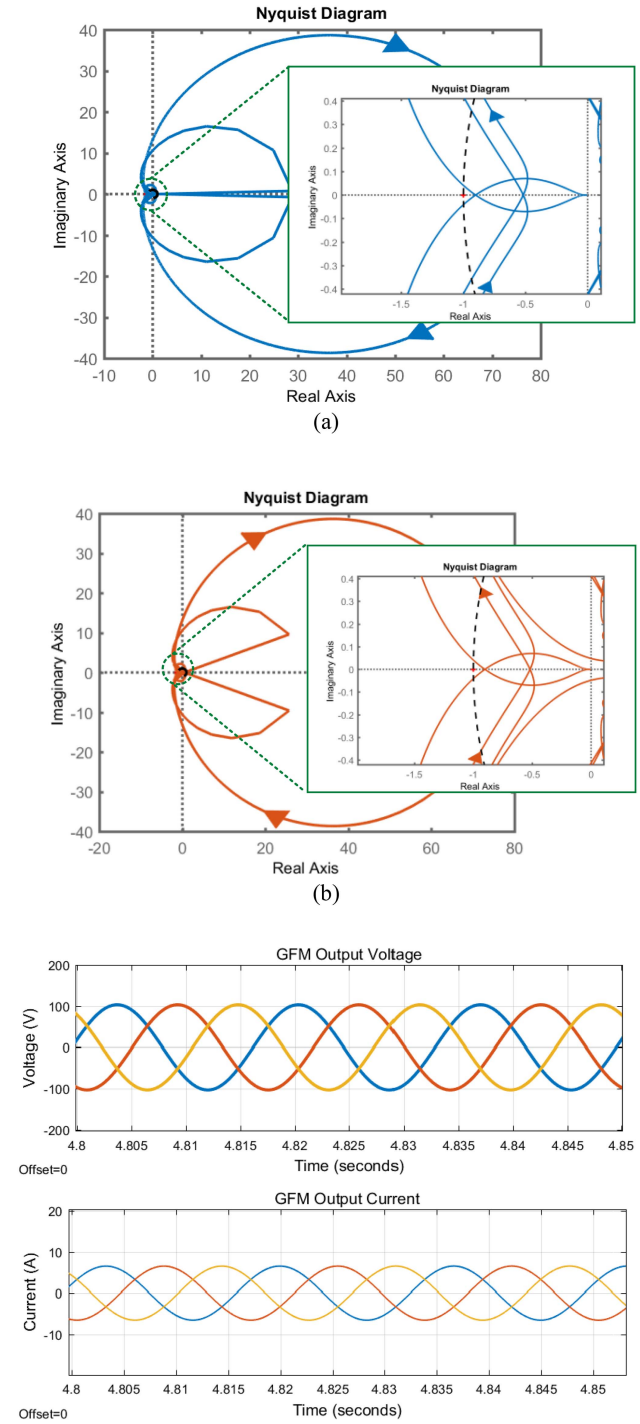

FIGURE 3. Stability analysis and simulations of GFMs under SCR = 5.6 (stable): (a) Eigenvalue 1 of $L_1(s)=Z_{o\_GFM\_1}(s)\,Y_g(s)$, (b) Eigenvalue 2 of $L_1(s)=Z_{o\_GFM\_1}(s)\,Y_g(s)$, and (c) Simulation results of output voltage and current.

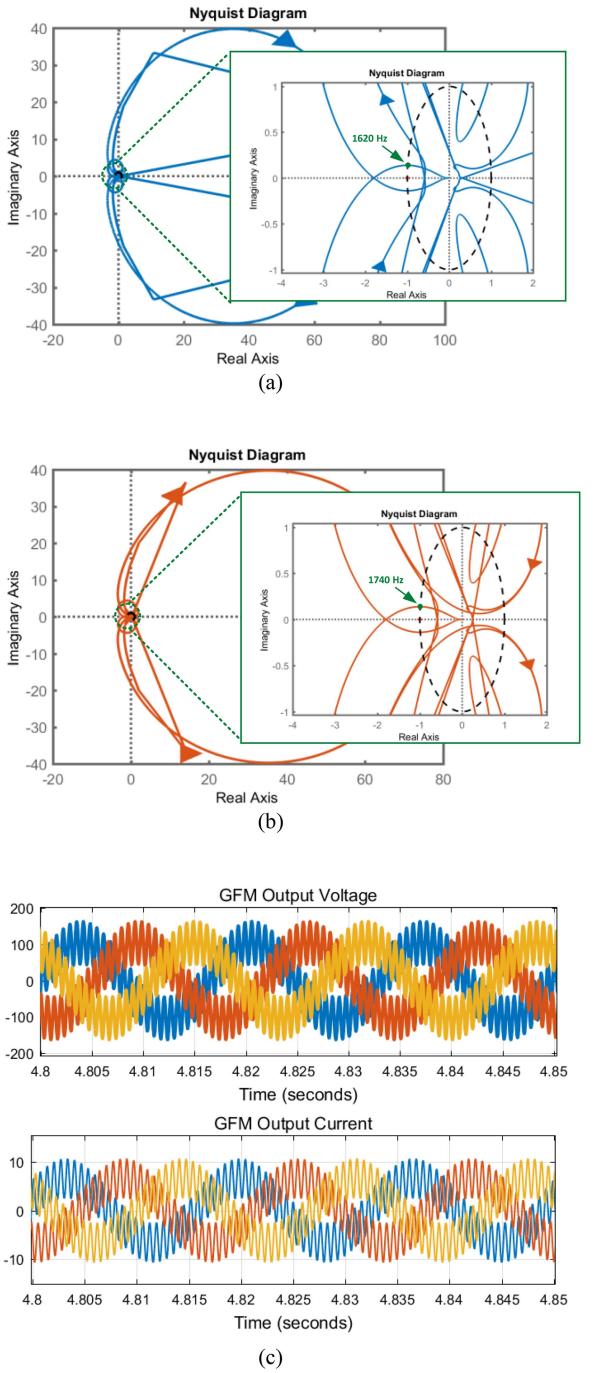

FIGURE 4. Stability analysis and simulations of GFMs under SCR = 11 (unstable): (a) Eigenvalue 1 of $L_1(s)=Z_{o\_GFM\_1}(s)\,Y_g(s)$, (b) Eigenvalue 2 of $L_1(s)=Z_{o\_GFM\_1}(s)\,Y_g(s)$, and (c) Simulation results of output voltage and current.

the system will start to exhibit some high-frequency harmonic instability issues. For example, when SCR = 11, the two eigenvalues of $\boldsymbol{L}_1(s)$ encircle (-1, j0) and the oscillation frequency is estimated to be 1.62 kHz (eigenvalue 1) and 1.74 kHz (eigenvalue 2) as shown in Fig. 4(a) and (b), which match the simulation results where both the output voltage and output current have such high-frequency harmonic oscillations. When SCR = 7.5, 15, and 22, the system will have similar harmonic instability issues. Also, since there are no RHP poles in $\boldsymbol{L}_1(s)$, the system stability could be determined directly by checking if there is any encirclement of (-1, j0) of the two eigenvalues of $\boldsymbol{L}_1(s)$.

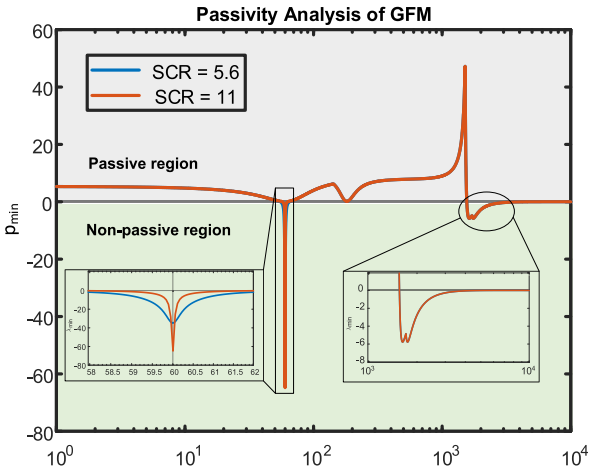

FIGURE 5. Passivity analysis of GFMs with basic control $Z_{o\_GFM\_1}(s)$ under SCR = 5.6 and 11.

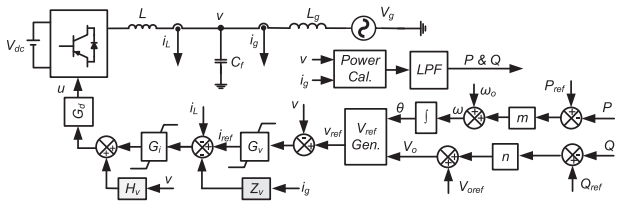

FIGURE 6. Control and circuit diagrams of GFMs with Z_v and H_v control blocks [15].

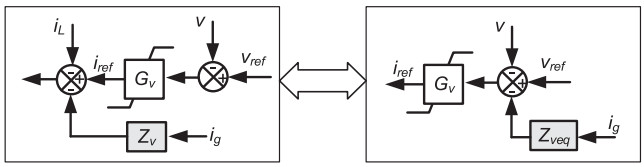

FIGURE 7. Manipulation of the virtual impedance control block.

C. PASSIVITY ANALYSIS OF GFMS

The reason why under different grid impedance, the system would have instability issues can be also analyzed through the passivity analysis of the impedance model of GFMs. For the MIMO transfer function matrix $\boldsymbol{Z_{o\_GFM}}(s)$, it is passive if it satisfies [19]:

1) all poles of $\boldsymbol{Z_{o\_GFM}}(s)$ are in the left-half plane;
2) $p_{min}[\boldsymbol{Z_{o\_GFM}}(j\omega) + \boldsymbol{Z^H_{o\_GFM}}(j\omega)] \geq 0$ for any $\omega \in (-\infty, \infty)$, where, p_{min} is the minimum eigenvalue of the impedance matrix across the whole frequency range and $\boldsymbol{Z^H_{o\_GFM}}$ is the conjugate transpose of $\boldsymbol{Z_{o\_GFM}}$.

According to the parameters in Table 1, the Bode diagram of the p_{min} of the impedance model of GFMs can be obtained under SCR = 5.6 and SCR = 11. As shown in Fig. 5, there will be two non-passive regions of the GFMs, one is near the system fundamental frequency, and the other is in the high-frequency range which is above 1 kHz. For the low-frequency non-passive region, it is a narrow frequency band, so if the droop gains are designed to be small enough, the low-frequency oscillations of the system could be avoided. For the high-frequency non-passive region which is mainly caused by the control delay block G_d, it is a wider non-passive region compared with the low-frequency one. And if no action was taken, instability issues may happen with different grid impedances, e.g., the simulation results under SCR = 11 in Fig. 4.

Note that the non-passive region in the impedance model means that instability issues might occur in this frequency band when interacting with other impedances in the system. Also, a passive system must be a stable system, but a stable system is not necessarily passive.

III. PROPOSED ONLINE-HARMONIC DETECTION-BASED SYSTEM STABILIZATION FUNCTION

A. POTENTIAL ISSUES OF EXISTING PASSIVITY-BASED CONTROL APPROACH FOR GFMS

As can be seen in Fig. 5, there is a high-frequency non-passive region where harmonic instability issues could occur. Therefore, if the high-frequency non-passive region is eliminated, then as a result, the harmonic instability issues can be avoided. Accordingly, a passivity-based linear control approach has been developed in [15] as shown in Fig. 6, where two extra control blocks are added to the system, one is a virtual impedance control block Z_v and the other is the capacitor voltage decoupling control block H_v. Additionally, the H_v and Z_v blocks should be calculated based on the control parameters and the circuit components as shown in (16) and (17). With the Z_v and H_v blocks, there will be no high-frequency harmonic instability issues under different grid conditions if ignoring the dynamics of the outer power loops [15].

$$Z_v = \frac{1 - K_{rv}L}{\left(\frac{2\pi f_{sw}}{6}\right)^2 LC_f - 1} \tag{16}$$

$$H_v = K_{pi}K_{pv} \tag{17}$$

However, it was found by the authors that although this Z_v and H_v-based method can help with system high-frequency stability issues, it might deteriorate the low-frequency stability if the power loop dynamics are considered.

To analyze such a phenomenon, the full-order model of the GFM in Fig. 6 needs to be derived first. To obtain the full-order model, a circuit manipulation is required that is moving the Z_v block from 'after the voltage control block G_v' to 'before the voltage control block G_v' with an equivalent block Z_{veq} as shown in Fig. 7.

Accordingly, the full-order model of GFM in Fig. 6 can be obtained as shown in Fig. 8, where Z_{o_ff} and G_{VVr_ff} consider the impact of H_v compared with Z_o in (9) and G_{vvr} in (10), respectively; and Z_{veq} depicts the impact of Z_v blocks on both power loops and inner voltage loops. Therefore, the full-order model $\boldsymbol{Z_{o\_GFM\_2}}(s)$ can be obtained as (18).

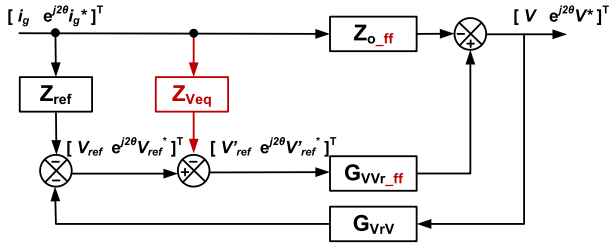

FIGURE 8. Full-order model of GFMs with control strategy in Fig. 6.

$$\boldsymbol{Z_{o\_GFM\_2}}(s) = (\boldsymbol{I} + \boldsymbol{G_{vvr\_ff}G_{VrV}})^{-1}\left(\boldsymbol{Z_{o\_ff}} + \boldsymbol{G_{vvr\_ff}}\left(\boldsymbol{Z_{ref}} + \boldsymbol{Z_{Veq}}\right)\right) \tag{18}$$

where,

$$\boldsymbol{Z_{o\_ff}}(s) = \begin{bmatrix} Z_{ov\_ff}(s) & 0 \\ 0 & Z_{ov\_ff}(s - 2j\omega_0) \end{bmatrix} \tag{19}$$

$$\boldsymbol{G_{VVr\_ff}}(s) = \begin{bmatrix} G_{vvr\_ff}(s) & 0 \\ 0 & G_{vvr\_ff}(s - 2j\omega_0) \end{bmatrix} \tag{20}$$

$$\boldsymbol{Z_{veq}}(s) = \begin{bmatrix} \frac{z_v}{G_v(s)} & 0 \\ 0 & \frac{z_v}{G_v(s-2j\omega_0)} \end{bmatrix} \tag{21}$$

$$Z_{ov\_ff}(s) = \frac{sL + G_iG_d}{LC_fs^2 + G_iG_dC_fs + (G_vG_i - H_v)G_d + 1} \tag{22}$$

$$G_{vvr\_ff}(s) = \frac{G_vG_iG_d}{LC_fs^2 + G_iG_dC_fs + (G_vG_i - H_v)G_d + 1} \tag{23}$$

Based on the derived impedance model, passivity analysis and stability analysis can be conducted. First, as shown in Fig. 9(a), the high-frequency non-passive region of $Z_{o\_GFM\_1}$ is eliminated in $Z_{o\_GFM\_2}$, which corresponds to the conclusions in [15] and the low-frequency passivity of Z_{o_GFM2} seems to be enhanced comparing with Z_{o_GFM2} due to the higher p_{min} in a wide frequency band. However, the non-passive regions near the system fundamental frequency of both Z_{o_GFM1} and Z_{o_GFM2} stay unchanged, which means the potential low-frequency instability issues still exist.

Second, the Nyquist diagrams of the eigenvalues of the return ratio matrices are obtained in Fig. 9(b) and (c). It can be observed that one of the eigenvalues of $\boldsymbol{L_1}(s)$ encircles the critical point with Z_{o_GFM1}, so the system is unstable with 1.74 kHz harmonics, which has also been shown in the simulation results in Fig. 4(b). While with Z_{o_GFM2}, there is no encirclement of the critical point (-1, j0) of one of the eigenvalues of $\boldsymbol{L_2}(s)$, which means that there is no right-half plane pole in the system. However, it can be observed that the gain margin is reduced from 4.6 dB at 62 Hz to 1.8 dB at 61.7 Hz. Hence, the system would have low-frequency oscillations at 61.7 Hz due to the lack of stability margin as shown by the simulation results in Fig. 10.

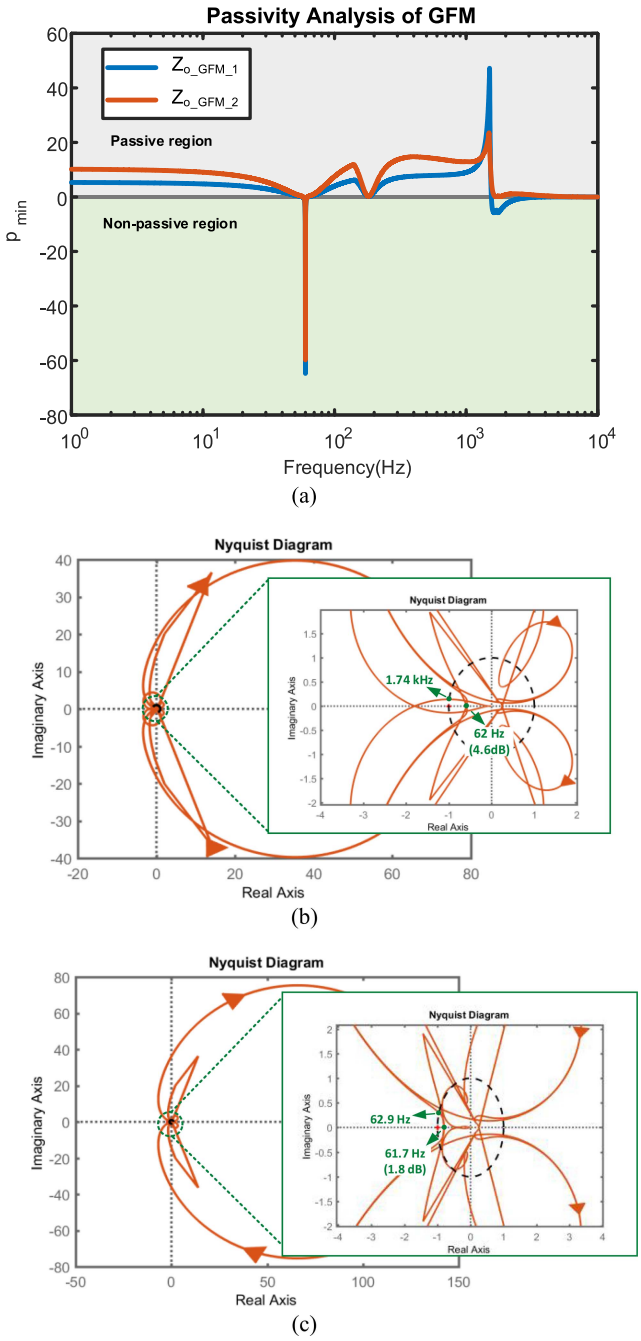

FIGURE 9. Passivity and stability analysis of GFMs with control strategy in Fig. 6 under SCR = 11: (a) Passivity analysis of $Z_{o\_GFM\_1}(s)$ and $Z_{o\_GFM\_2}(s)$, (b) Eigenvalue 2 of $L_1(s) = Z_{o\_GFM\_1}(s)\,Y_g(s)$, and (c) Eigenvalue 2 of $L_2(s) = Z_{o\_GFM\_2}(s)Y_g(s)$.

More cases under different grid conditions are summarized in Table 2. It is shown that with the basic control method in Fig. 1, the system might have high-frequency harmonic instability issues with predefined stable low-frequency dynamics. On the other hand, it is found that although the harmonic instability issues can be eliminated with Z_v and H_v-based method (as shown in Fig. 6), low-frequency oscillations might occur as a side effect. And this low-frequency instability issue

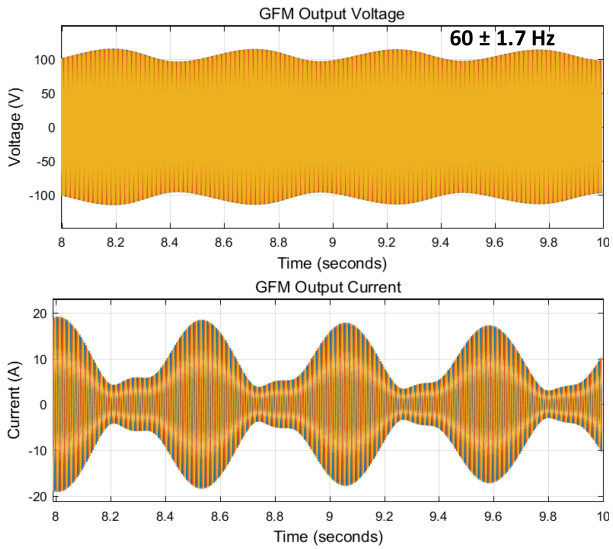

FIGURE 10. Low-frequency oscillations with control diagrams in Fig. 6 under SCR = 11.

TABLE 2. Simulation and Analysis Results of GFMs Under Various Grid Conditions

Grid SCRs	Control in Fig. 1 $Z_{o\_GFM\_1}$	Control in Fig. 6 $Z_{o\_GFM\_2}$
5.6	Stable	Stable
7.5	HF harmonics (1.69 kHz)	LF oscillations (60 ± 2.4 Hz)
11	HF harmonics (1.74 kHz)	LF oscillations (60 ± 1.7 Hz)
15	HF harmonics (1.79 kHz)	LF oscillations (60 ± 1.2 Hz)
22	HF harmonics (1.89 kHz)	LF oscillations (60 ± 1.1 Hz)

is mainly caused by an insufficient stability margin near the system fundamental frequency.

To eliminate the low-frequency oscillations and keep the high-frequency region non-passive with the passivity-based control approach in Fig. 6, online tuning for a smaller droop gain or an angle droop compensation block [20] can be used. However, this is not a general solution since if the outer power loop is implemented with other control, like the dVOC approach [6], the impact of Z_v on the system low-frequency stability needs to be examined again to find corresponding solutions. Therefore, it is desirable to have a method that can help to solve high-frequency harmonic issues without affecting the predefined low-frequency dynamics of the system.

B. PROPOSED ONLINE HARMONIC DETECTION-BASED SSF

To ensure system stability under various grid conditions, the desired control approach for GFMs should be able to adaptively adjust the controller to eliminate the harmonic instability phenomena, and also not to affect the predefined system in the low-frequency region as discussed in Section III-A. The key is to only add a system stabilization function (SSF) in the inner current loop; therefore, only the high-frequency characteristics will be improved while the low-frequency dynamics will not be affected which are mainly determined by the outer voltage and power loop.

Accordingly, an SSF for GFMs is proposed as shown in Fig. 11. Specifically, when connecting the GFM to an existing grid, if the system is stable, no action will be needed; but if there are harmonic instability issues, the system stabilization function embedded in the controller of GFMs should start to stabilize the system by passivating the inverter impedance at the system harmonic resonant frequency. All the symbols used in Fig. 11 are summarized in Table 3.

In the proposed SSF, an online harmonic detection module is operated first. A Fast Fourier transform (FFT) block analyzes the harmonic component in the output voltage of the GFMs by removing the fundamental frequency component through a band-pass filter in the sampled data. The maximum value (i.e., the magnitude of the resonance component, ResMag) and the frequency index (i.e., the frequency of the resonant frequency order, ResOrder) of the harmonic component would be identified.

Then, with the detected magnitude (ResMag) and frequency index (ResOrder) of the harmonic resonant component, a logic calculation block will be executed when the external enable signal (En_Ext) is 1 (i.e., En_Ext = 1, enable the SSF; En_Ext = 0, disable the SSF). If ResMag exceeds the preset magnitude threshold (ResThreshold) and ResOrder > 0, the internal enable signal (En_Int) for SSF will then be set high. By considering every possibility for the sampled data and system working conditions, four states (S1 – S4)

TABLE 3. Meanings of Different Symbols in Fig. 11

Symbols	Meanings
En_Ext	External enable signal for K_{FF} compensation block
ResThreshold	The preset threshold for the magnitude of the detected resonant component
ResMag	The calculated magnitude of the resonant component through the FFT algorithm
ResOrder	Frequency index of the resonant component through the FFT algorithm
Res_Flag 0&1	The transition of the states and Res_Flag0 is the value of Res_Flag1 in the previous step
En_Int	Internal enable signal for K_{FF} compensation block. In S2- 4, En_Int = 1; otherwise, En_Int = 0.
Comp_ResOrder	Frequency order of the resonant component that is used for K_{FF} calculation
Freq_update	Resonant frequency updating signal. If Freq_update = 0, the calculated resonant frequency will remain the same as the previous value; if Freq_update = 1, the calculated resonant frequency will be updated to the current calculation result.

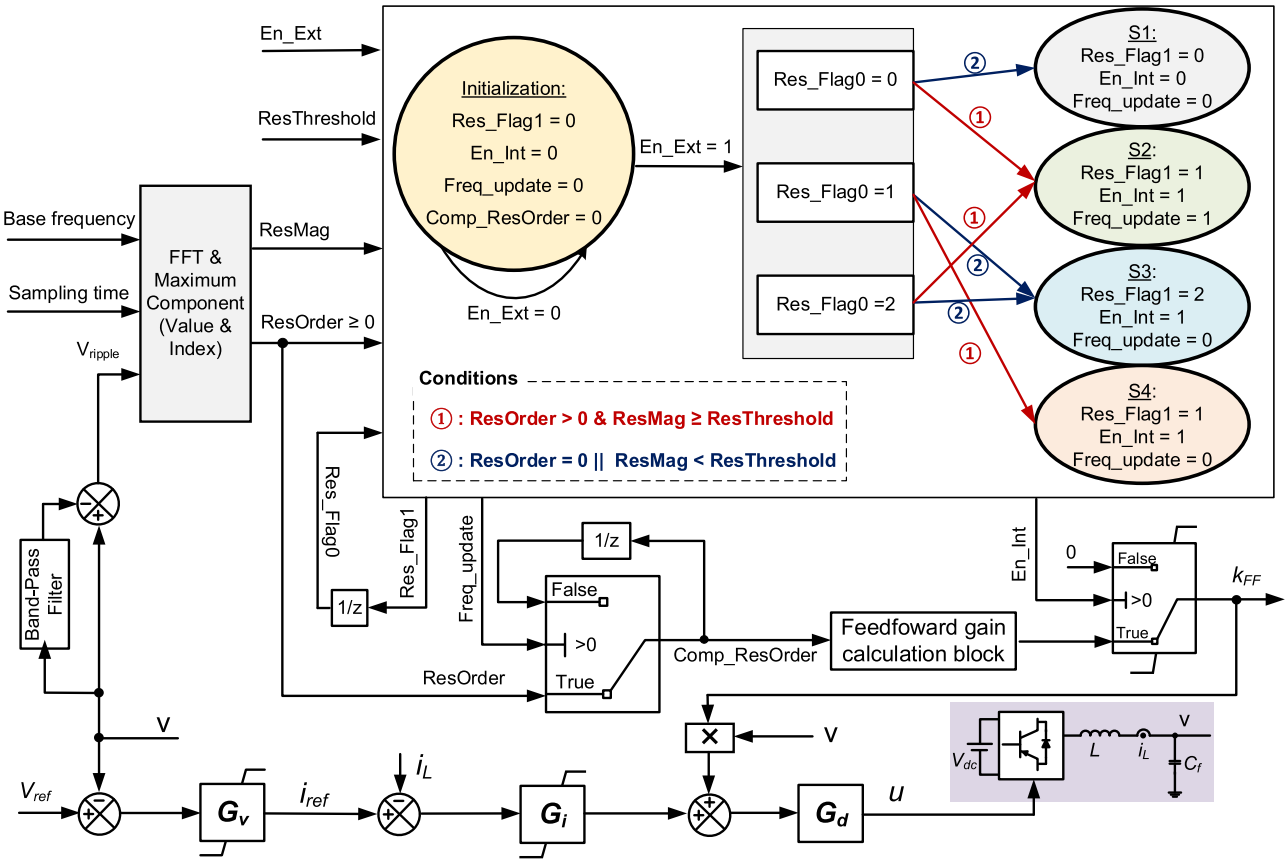

FIGURE 11. Proposed online harmonic detection-based SSF for GFMs.

are considered, and the values of the internal enabling signal (En_Int), the resonance flag (Res_Flag1), and the frequency updating signal (Freq_update) need to be updated accordingly as shown below:

S1: Res_Flag1 = 0, En_Int = 0, and Freq_update = 0;
S2: Res_Flag1 = 1, En_Int = 1, and Freq_update = 1;
S3: Res_Flag1 = 2, En_Int = 1, and Freq_update = 0;
S4: Res_Flag1 = 1, En_Int = 1, and Freq_update = 0.

Also, moving among different states needs to follow the direction which meets one of these two conditions indicated by the arrows in Fig. 11:

Condition ①: ResOrder > 0 and ResMag ≥ ResThreshold
Condition ②: ResOrder = 0 or ResMag < ResThreshold

If the Freq_update signal is 1, then the measured harmonic frequency order (ResOrder) will be passed to Comp_ResOrder for the feedforward gain calculation. If the Freq_update signal is 0, the Comp_ResOrder would remain as the value in the previous calculation cycle. Once the En_Int is 1, the calculated voltage feedforward gain K_{FF} will form a voltage feedforward block and will be added to the inner current control loop for the system stabilization; otherwise, $K_{FF} = 0$, and no compensation is executed.

For the feedforward gain calculation block, it is developed to make the inverter impedance passive at the harmonic resonant frequency of the system so that the harmonic instability issues can be eliminated. Accordingly, the output impedance model of GFMs $\boldsymbol{Z_{o\_GFM\_3}}$ can be obtained as (24) by considering the K_{FF} block, where $\boldsymbol{Z_{o\_kFF}}$ is given in (25), $\boldsymbol{G_{VVr\_KFF}}$ is given in (26), Z_{ov_kFF} is given in (27) and G_{vvr_kFF} is given in (28).

$$\boldsymbol{Z_{o\_GFM\_3}}(s) = (\boldsymbol{I} + \boldsymbol{G_{VVr\_kFF}}\boldsymbol{G_{VrV}})^{-1}\left(\boldsymbol{Z_{o\_kFF}} + \boldsymbol{G_{VVr\_kFF}}\boldsymbol{Z_{ref}}\right) \quad (24)$$

where,

$$\boldsymbol{Z_{o\_kFF}}(s) = \begin{bmatrix} Z_{ov\_kFF}(s) & 0 \\ 0 & Z_{ov\_kFF}(s - 2j\omega_0) \end{bmatrix} \quad (25)$$

$$\boldsymbol{G_{VVr\_kFF}}(s) = \begin{bmatrix} G_{vvr\_kFF}(s) & 0 \\ 0 & G_{vvr\_kFF}(s - 2j\omega_0) \end{bmatrix} \quad (26)$$

$$Z_{ov\_kFF}(s) = \frac{sL + G_iG_d}{LC_fs^2 + G_iG_dC_fs + (G_vG_i - k_{FF})G_d + 1} \quad (27)$$

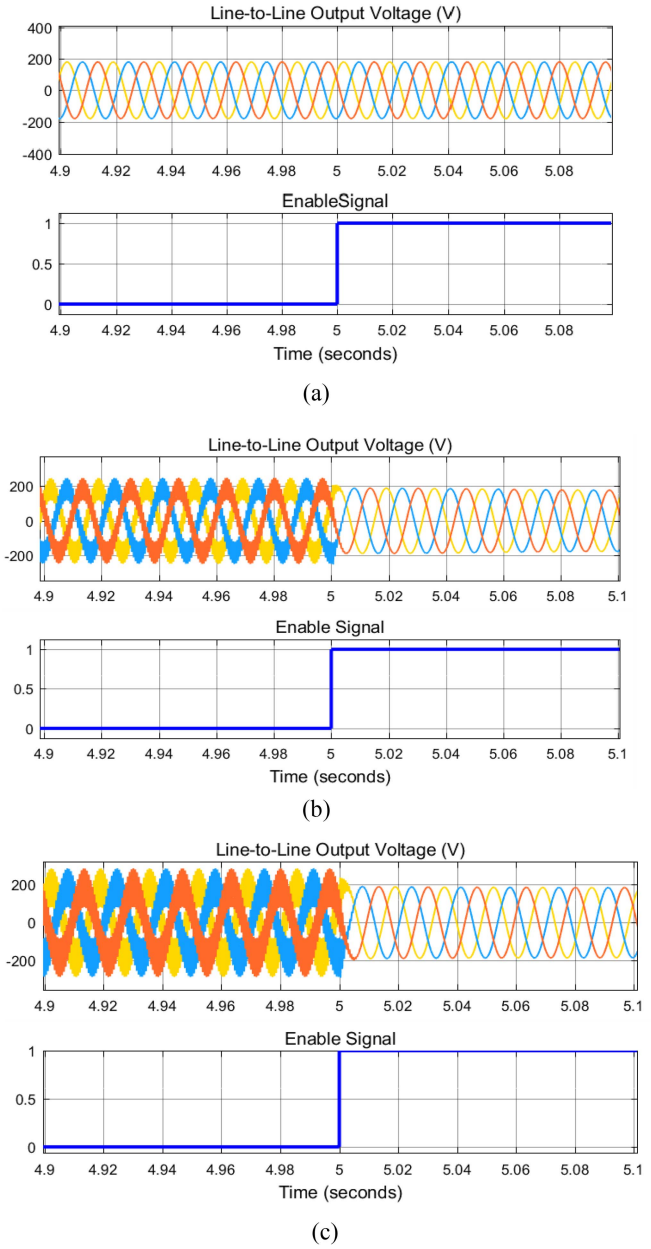

FIGURE 12. Simulation results (a) SCR = 5.6, (b) SCR= 7.5, and (c) SCR = 15.

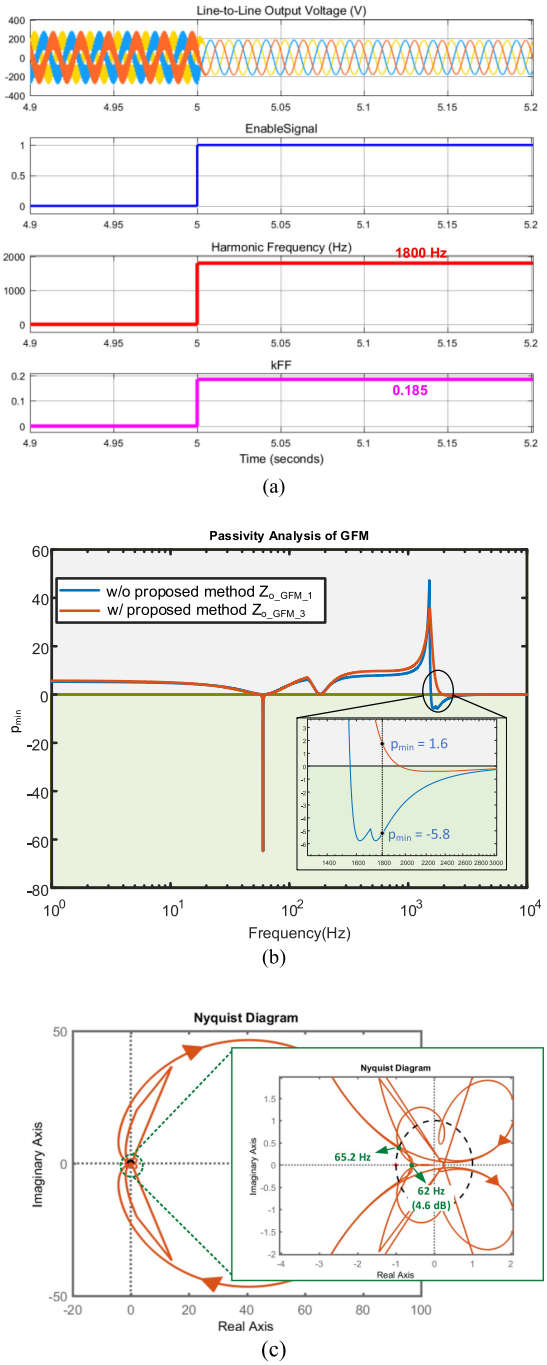

FIGURE 13. Proposed method under SCR = 11: (a) Simulation results, (b) Passivity comparisons between the proposed method $Z_{o\_GFM\_3}(s)$ and the basic control approach $Z_{o\_GFM\_1}(s)$, and (c) Eigenvalue 2 of $L_3(s) = =Z_{o\_GFM\_3}(s)Y_g(s)$.

$$G_{vvr\_kFF}(s) = \frac{G_v G_i G_d}{LC_f s^2 + G_i G_d C_f s + (G_v G_i - k_{FF})G_d + 1} \tag{28}$$

Since the K_{FF} block is added in the inner current loop, and the harmonic instability issue is considered here, the impedance model can be simplified as (27) by ignoring the outer power loop. Then, to make the inverter impedance passive at the resonant frequency ω_{res}, the real part of the inverter impedance model should be non-negative. As shown in (29), the sign of the real part of $Z_{ov\_kFF}(j\omega)$ is mainly determined by A, where A is given in (30). Therefore, the critical value of K_{FF} is derived as shown in (31), where L is the output inductance, K_{pi} or K_{pv} is the current or voltage controller proportional gain, K_{rv} is the voltage controller resonance gain, and T_d is converter control delay. With this feedforward gain, the inverter impedance would be passive at ω_{res}. More details about the derivation of critical value for K_{FF} can be found in the Appendix. Note that an extra stability margin can be

reserved by multiplying k_{FF} with some constant gain, e.g., 1.2 or 1.3.

$$sgn\left\{Re\left\{Z_{oV_{kFF}}\left(\omega_{res}\right)\right\}\right\} = sgn\ \{A\} \geq 0 \tag{29}$$

$$A = K_{pi}\left(1 - K_{rv}L\right)\cos\left(\omega_{res}T_d\right) + K_{pv}K_{pi}^2 - \omega_{res}LK_{pv}K_{pi}sin\left(\omega_{res}T_d\right) + k_{FF}\left(\omega_{res}Lsin\left(\omega_{res}T_d\right) - K_{pi}\right) \tag{30}$$

$$K_{FF} = K_{pi}K_{pv} + \frac{K_{pi}\left(1 - K_{rv}L\right)\cos\left(\omega_{res}T_d\right)}{-\omega_{res}L\sin\left(\omega_{res}T_d\right) + K_{pi}} \tag{31}$$

IV. VALIDATIONS OF PROPOSED SSF FOR GFMS

A. SIMULATION TESTS

To validate the effectiveness of the proposed approach, a grid-connected GFM with the proposed SSF is implemented in MATLAB/Simulink. The control parameters and system working conditions are the same as those in Table 1.

Fig. 12 shows the simulation results under different grid conditions. It can be seen that when there are no harmonic stability issues, even though the external-enabling instruction signal (En_Ext) is enabled at t = 5 *s*, no action would be taken, and the system remains stable as shown in Fig. 12(a). From Fig. 12(b) and (c), it can be observed that once there are high-frequency harmonics in the system, when the SSF is enabled at t = 5 s, the harmonic components can be eliminated, and the system can be stabilized.

Details of control actions can be seen with the example under SCR = 11 below. As shown in Fig. 13(a), before enabling the proposed SSF, the harmonic frequency is detected to be 1.8 kHz, and after enabling the SSF at t = 5 *s*, the system can be stabilized with a calculated k_{FF} value.

Further analysis can be conducted with the derived impedance model in (24) by substituting the calculated feed-forward gain value. As shown in Fig. 13(b), without the proposed method (i.e., the control in Fig. 1), the inverter impedance is non-passive at 1.8 kHz with p_{min} = -5.8; while with the proposed approach, the system can be passive at 1.8 kHz with p_{min} = 1.6. It can also be observed that the proposed approach will not affect the low-frequency dynamics since the passivity indices for both $\boldsymbol{Z_{o\_GFM\_1}}$ and $\boldsymbol{Z_{o\_GFM\_3}}$ remain the same in the low-frequency range.

Fig. 13(c) shows the impedance-based stability analysis results of the system under SCR = 11 based on the eigenvalues of $\boldsymbol{L_3}(s)$. It can be seen that with the proposed method, there will be no encirclement of the critical point at high frequency. And the low-frequency dynamics will not be affected since the Nyquist diagrams of the eigenvalues with or without the proposed method remain the same at the low-frequency range as shown in Figs. 13(c) and 9(b), respectively.

B. EXPERIMENTAL TESTS

An experimental setup as shown in Fig. 14 is built for further verification. As can be seen, two converters are connected, with one converter working as the grid emulator with open-loop control, and the other converter working as a GFM

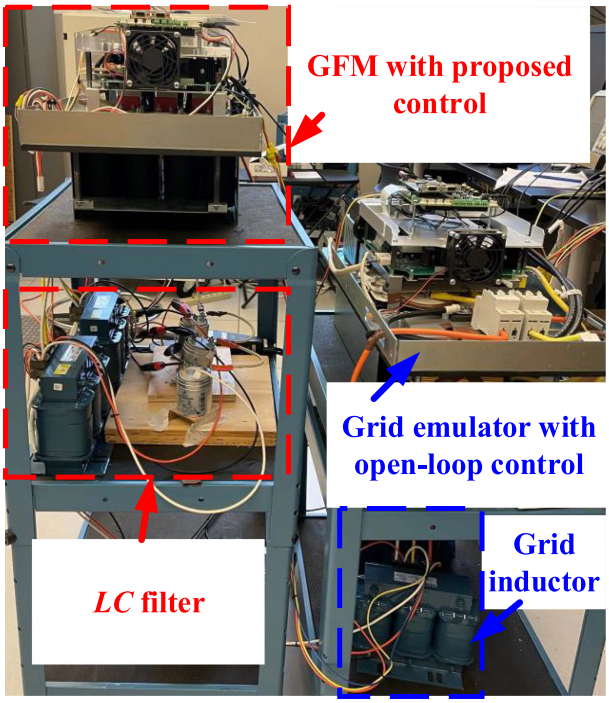

FIGURE 14. Experimental setup.

TABLE 4. Circuit and Control Parameters of GFMs and Grid Conditions

Variables	Value	Variables	Value
GFM voltage RMS value V_o	50 V	Fundamental frequency f_0	60 Hz
Dc voltage V_{dc}	130 V	Switching frequency f_{sw}	10 kHz
LC filter capacitance *L*, *C*	1.2 mH, 10 μF	Power references P_0, Q_0	600 W, 0 Var
Control delay T_d	$1.5/f_{sw}$	Current *P* control K_{pi}	6.9
Grid side impedance L_g	4.8 mH	Voltage PR control K_{pv}, K_{rv}	0.01, 50

with the proposed SSF. The system working conditions and control parameters are listed in Table 4. Fig. 15 shows the test results of GFMs with the basic control structure (i.e., the circuit in Fig. 1), it can be seen that there are harmonic instability issues in the output voltage. With Z_v and H_v-based control, there would be no high-frequency harmonics, but low-frequency oscillations could be observed as shown in Fig. 16. While with the proposed SSF, the high-frequency harmonic instability issues can be eliminated once SSF is enabled, and low-frequency stability is also maintained as shown in Fig. 17.

V. CONCLUSION

In this paper, it is found that the Z_v block, which is originally designed for the passivation of the impedance model of GFMs

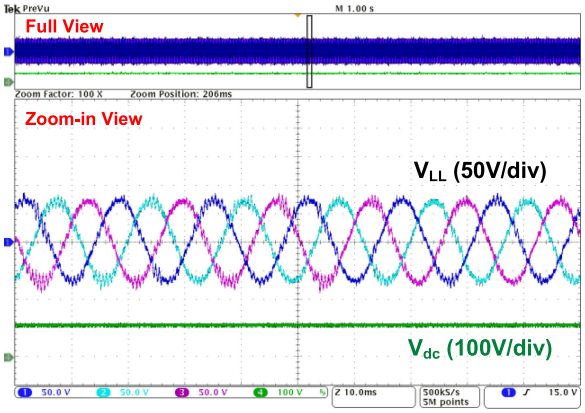

FIGURE 15. Experimental results with basic control in Fig. 1.

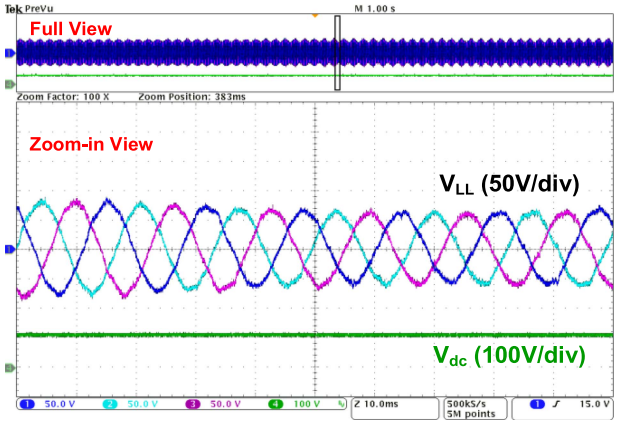

FIGURE 16. Experimental results with the control in Fig. 6.

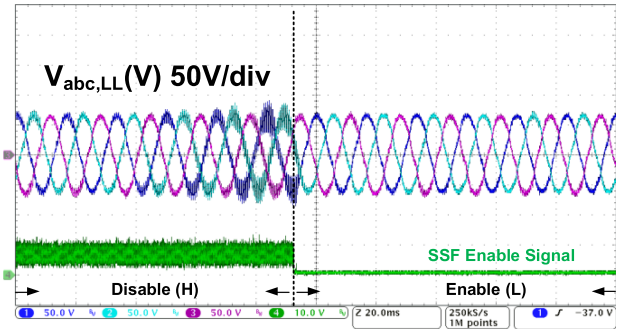

FIGURE 17. Experimental results with the proposed SSF approach.

at the high-frequency range to improve system harmonic stability, could reduce the system low-frequency stability margin and cause low-frequency stability issues. Therefore, instead of using the offline approach to design the inverter to be passive at high frequency, this paper proposes an online approach to identify the resonant frequency of the harmonic instabilities in the system first, and then perform the passivity compensation at this identified resonant frequency. As a result, the harmonic instability issues in the system can be eliminated; in the meantime, the predefined low-frequency dynamics will not be affected. The proposed approach has been validated by simulation and experimental tests.

APPENDIX

By substituting $s = j\omega_{res}$ into (27), the following equation can be obtained:

$$Re\left\{Z_{oV\_kFF}\left(\omega_{res}\right)\right\} = Re\left\{\frac{Num}{Den}\right\}$$

where,

$$Num = j\omega_{res}L + K_{pi}\left[\cos\left(\omega_{res}T_d\right) - jsin\left(\omega_{res}T_d\right)\right]$$

$$\begin{aligned} Den = & -LC_f\omega_{res}^2 + j\omega_{res}K_{pi}\left[\cos\left(\omega_{res}T_d\right) - jsin\left(\omega_{res}T_d\right)\right]C_f \\ & + \left[\left(K_{pv} - j\frac{K_{rv}}{\omega_{res}}\right)K_{pi} - k_{FF}\right] \\ & \left[\cos\left(\omega_{res}T_d\right) - jsin\left(\omega_{res}T_d\right)\right] + 1 \end{aligned}$$

Then, $Re\{\frac{Num}{Den}\}$ can be further calculated as $\frac{Z}{X^2+Y^2}$, where,

$$\begin{aligned} Z = & K_{pi}\left(1 - K_{rv}L\right)\cos\left(\omega_{res}T_d\right) + K_{pv}K_{pi}^2 \\ & - \omega_{res}LK_{pv}K_{pi}sin\left(\omega_{res}T_d\right) \\ & + k_{FF}\left(\omega_{res}Lsin\left(\omega_{res}T_d\right) - K_{pi}\right), \end{aligned}$$

$$\begin{aligned} X = & 1 - LC_f\omega_{res}^2 + \omega_{res}K_{pi}C_fsin\left(\omega_{res}T_d\right) \\ & + K_{pv}K_{pi}\cos\left(\omega_{res}T_d\right) - \frac{K_{pi}K_{rv}}{\omega_{res}}sin\left(\omega_{res}T_d\right) \\ & - k_{FF}\cos\left(\omega_{res}T_d\right), \end{aligned}$$

$$\begin{aligned} Y = & \omega_{res}K_{pi}C_f\cos\left(\omega_{res}T_d\right) - \frac{K_{pi}K_{rv}}{\omega_{res}}\cos\left(\omega_{res}T_d\right) \\ & - K_{pv}K_{pi}sin\left(\omega_{res}T_d\right) + k_{FF}sin\left(\omega_{res}T_d\right). \end{aligned}$$

Since $X^2 + Y^2 > 0$, the sign of $\{Re\{Z_{oV\_kFF}(\omega_{res})\}$ will be mainly determined by sgn $\{Z\}$. To achieve sgn $\{Z\} \geq 0$, the critical value for K_{FF} can then be obtained as (31).

REFERENCES

[1] A. Tuckey and S. Round, "Grid-forming inverters for grid-connected microgrids: Developing 'good citizens' to ensure the continued flow of stable, reliable power," *IEEE Electrific. Mag.*, vol. 10, no. 1, pp. 39–51, Mar. 2022.

[2] Q.-C. Zhong, "Power-electronics-enabled autonomous power systems: Architecture and technical routes," *IEEE Trans. Ind. Electron.*, vol. 64, no. 7, pp. 5907–5918, Jul. 2017.

[3] J. Rocabert, A. Luna, F. Blaabjerg, and P. Rodríguez, "Control of power converters in AC microgrids," *IEEE Trans. Power Electron.*, vol. 27, no. 11, pp. 4734–4749, Nov. 2012.

[4] W. Du et al., "A comparative study of two widely used grid-forming droop controls on microgrid small-signal stability," *IEEE J. Emerg. Sel. Topics Power Electron.*, vol. 8, no. 2, pp. 963–975, Jun. 2020.

[5] Q.-C. Zhong, "Virtual synchronous machines: A unified interface for grid integration," *IEEE Power Electron. Mag.*, vol. 3, no. 4, pp. 18–27, Dec. 2016.
[6] G. Seo, M. Colombino, I. Subotic, B. Johnson, D. Groß, and F. Dörfler, "Dispatchable virtual oscillator control for decentralized inverter-dominated power systems: Analysis and experiments," in *Proc. IEEE Appl. Power Electron. Conf. Expo.*, 2019, pp. 561–566.
[7] M. Lu, S. Dutta, V. Purba, S. Dhople, and B. Johnson, "A grid-compatible virtual oscillator controller: Analysis and design," in *Proc. IEEE Energy Convers. Congr. Expo.*, 2019, pp. 2643–2649.
[8] N. Hatziargyriou et al., "Definition and classification of power system stability -revisited & extended," *IEEE Trans. Power Syst.*, vol. 36, no. 4, pp. 3271–3281, Jul. 2021.
[9] L. Kong, Y. Xue, L. Qiao, and F. Wang, "Review of small-signal converter-driven stability issues in power systems," *IEEE Open Access J. Power Energy*, vol. 9, pp. 29–41, 2022.
[10] J. Shair, H. Li, J. Hu, and X. Xie, "Power system stability issues, classifications and research prospects in the context of high-penetration of renewables and power electronics," *Renewable Sustain. Energy Rev.*, vol. 145, 2021, Art. no. 111111.
[11] Y. Xue et al., "On a future for smart inverters with integrated system functions," in *Proc. IEEE Int. Symp. Power Electron. Distrib. Gener. Syst.*, 2018, pp. 1–8.
[12] W. Cao, Y. Ma, and F. Wang, "Adaptive impedance compensation of inverters for stable grid integration based on online resonance detection," in *Proc. IEEE Appl. Power Electron. Conf. Expo.*, 2019, pp. 3151–3158.
[13] L. Harnefors, X. Wang, A. G. Yepes, and F. Blaabjerg, "Passivity-based stability assessment of grid-connected VSCs—An overview," *IEEE J. Emerg. Sel. Topics Power Electron.*, vol. 4, no. 1, pp. 116–125, Mar. 2016.
[14] J. Fang, X. Li, H. Li, and Y. Tang, "Stability improvement for three-phase grid-connected converters through impedance reshaping in quadrature-axis," *IEEE Trans. Power Electron.*, vol. 33, no. 10, pp. 8365–8375, Oct. 2018.
[15] Y. Liao, X. Wang, and F. Blaabjerg, "Passivity-based analysis and design of linear voltage controllers for voltage-source converters," *IEEE Open J. Ind. Electron. Soc.*, vol. 1, pp. 114–126, 2020.
[16] H. Yu, M. A. Awal, H. Tu, Y. Du, S. Lukic, and I. Husain, "Passivity-oriented discrete-time voltage controller design for grid-forming inverters," in *Proc. IEEE Energy Convers. Congr. Expo.*, 2019, pp. 469–475.
[17] M. Cespedes and J. Sun, "Adaptive control of grid-connected inverters based on online grid impedance measurements," *IEEE Trans. Sustain. Energy*, vol. 5, no. 2, pp. 516–523, Apr. 2014.
[18] Y. Liao, X. Wang, F. Liu, K. Xin, and Y. Liu, "Sub-synchronous control interaction in grid-forming VSCs with droop control," in *Proc. IEEE Workshop Electron. Grid*, 2019, pp. 1–6.
[19] J. U. Liceaga-Castro, I. I. Siller-Alcalá, E. Liceaga-Castro, and L. A. Amézquita-Brooks, "MIMO passive control systems are not necessarily robust," *J. Control Sci. Eng.*, vol. 2015, 2015, Art. no. 508102.
[20] L. Kong, Y. Xue, L. Qiao, and F. F. Wang, "Angle droop design for grid-forming inverters considering impacts of virtual impedance control," presented at the IEEE Energy Convers. Congr. and Expo., 2021, pp. 1006–1013.